Supporting Information for:

The Dealloying-Lithiation/Delithiation-Realloying Mechanism of Breithauptite (NiSb) Nanocrystals Embedded Nanofabric Anode for Flexible Li-ion Batteries

Renpeng Chen,[a] Xiaolan Xue,[a] Jingyu Lu,[a] Tao Chen,[a] Yi Hu,[a] Lianbo Ma,[a] Guoyin Zhu,[a] and Zhong Jin[a,b]*

[a] *Key Laboratory of Mesoscopic Chemistry of MOE, Jiangsu Key Laboratory of Advanced Organic Materials, School of Chemistry and Chemical Engineering, Nanjing University, Nanjing 210023, China.*

[b] *Shenzhen Research Institute of Nanjing University, Shenzhen 518063, China.*

*Address correspondence to zhongjin@nju.edu.cn

Table S1. Comparison of lithium storage performances of NiSb@NCNFs with other Sb-based electrode materials reported in previous literatures.

Ref.	Electrode material	Preparation method	Voltage range (V)	Current density (mA g^{-1})	Cycle number	Specific capacity (mAh g^{-1})
This work	**NiSb@NCNFs**	**Electrospinning method**	**0.01–3.0**	**100**	**50**	**720**
				1000	**100**	**610**
				2000	**2000**	**510**
30	NiSb nanoparticles	Solvothermal method	0.05–1.5	20	20	~165
31	$TiSb_2$ nanoparticles	High-temperature sintering	0.05–1.5	552	100	275
	$NbSb_2$ nanopatricles			478		90
32	$CoSb_3$ nanoparticles	Solvothermal method	0.05–1.5	20	10	257
33	$CoSb_2$ nanoparticles	Solvothermal method	0.05–1.5	20	20	551.3
34	CoSb nanowire arrays	Pulsed electrodeposition	0.05–4.5	60	10	200
35	Zn_4Sb_3 nanotubes	Chemical vapor deopsition	0.01–2.0	100	100	450
36	NiSb hollow nanospheres	Galvanic replacement	0.01–2.0	100	50	432
37	NiSb-Al_2O_3-C nanocomposite	High-energy mechanical milling	0–2.0	100	1000	280
38	Cu_2Sb-Al_2O_2-C nanocomposite	Mechanochemical reduction	0–2.0	100	500	456
39	$FeSb_2$-Al_2O_3-C	High-energy mechanical milling	0–2.0	100	500	350

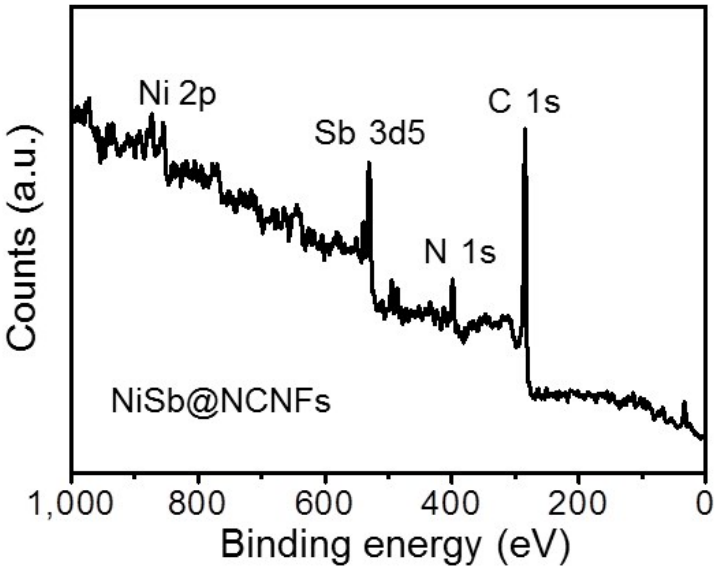

Fig. S1 Survey XPS spectrum of NiSb@NCNFs.

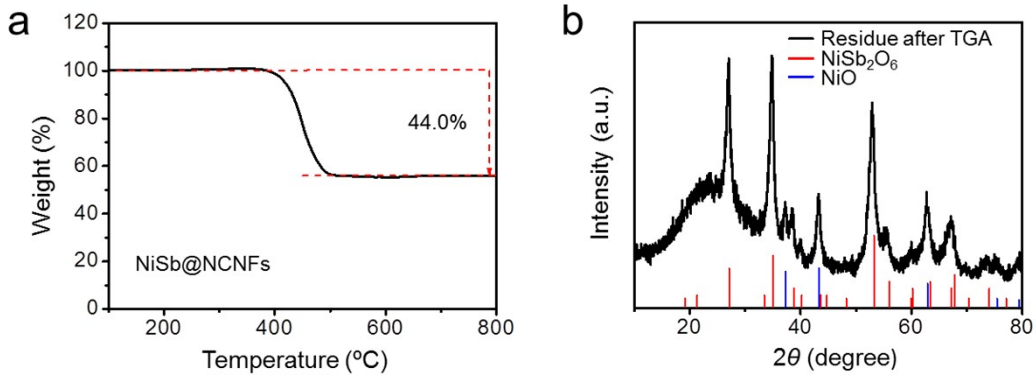

Fig. S2 (a) TGA curve of NiSb@NCNFs measured in air from room temperature to 800 °C with a heating rate of 5 °C min^{-1}. (b) XRD pattern of the powdery residue of NiSb@NCNFs after TGA test compared with the standard XRD patterns of $NiSb_2O_6$ and NiO.

In the TGA curve of Fig. S2a, the weight change should be ascribed to the thermal decomposition of NCNFs and the oxidation of NiSb. The C and N species in NCNFs were oxidized to gaseous products after heating. The weight retention of the powdery residue after TGA test is 56.0 wt.%. According to the XRD pattern of the solid residue (Fig. S2b), the NiSb nanocrystals were oxidized to NiO and $NiSb_2O_6$. Moreover, the ICP-OES analysis indicates that the atomic ratio of Ni:Sb is nearly 1:1. Therefore, the weight ratio of NiSb in the NiSb@NCNFs can be calculated from the following equation:

$$(m_{Total} \times \eta_{NiSb})/M_{NiSb} = m_{NiO}/M_{NiO} + m_{NiSb2O6}/M_{NiSb2O6}$$

where m_{Total} is the initial total weight of NiSb@NCNFs, η_{NiSb} is the weight ratio of NiSb in NiSb@NCNFs, m_{NiO} and $m_{NiSb2O6}$ are the weight of NiO and $NiSb_2O_6$ in the residue after TGA, respectively. M_{NiSb}, M_{NiO} and $M_{NiSb2O6}$ are the mole weights of NiSb, NiO and $NiSb_2O_6$, respectively. In this way, the η_{NiSb} can be calculated to be ~42.7 wt.%.

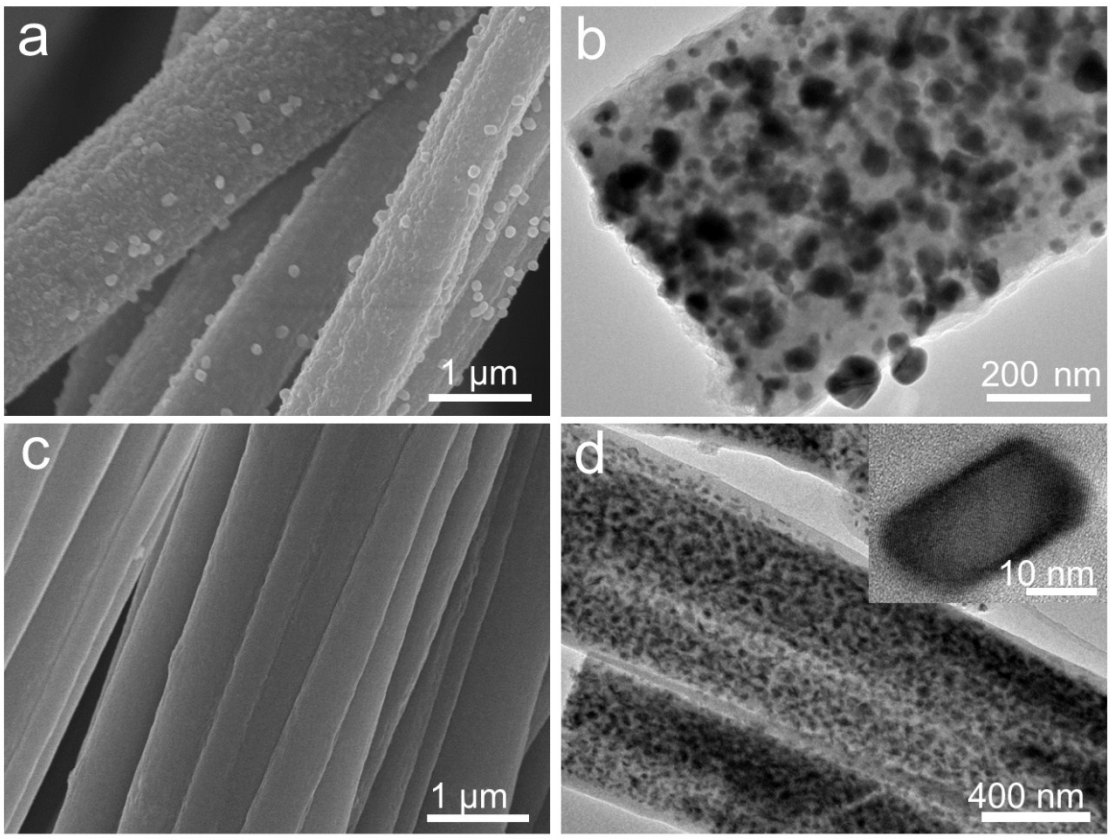

Fig. S3 (a) SEM and (b) TEM images of the Ni@NCNFs control sample. (c) SEM and (d) TEM images of the Sb@NCNFs control sample.

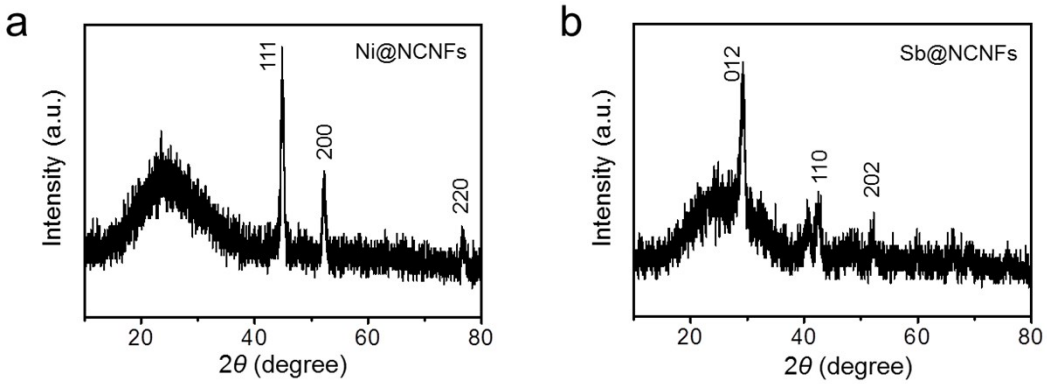

Fig. S4 XRD patterns of (a) Ni@NCNFs and (b) Sb@NCNFs control samples.

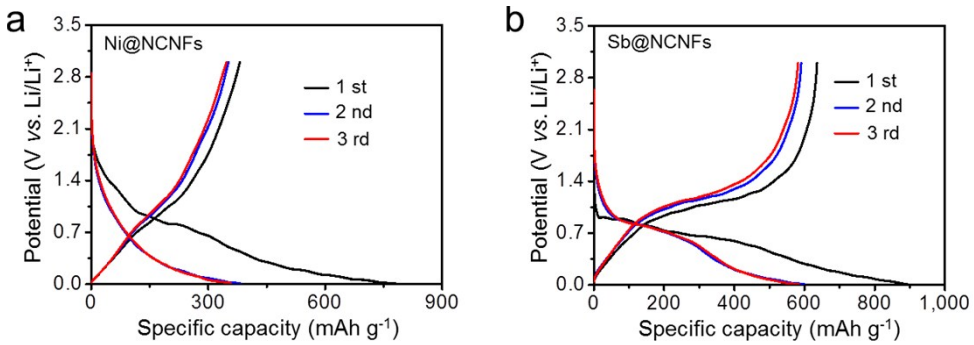

Fig. S5 Discharge-charge profiles of (a) Ni@NCNFs and (b) Sb@NCNFs control samples at 100 mA g^{-1}.

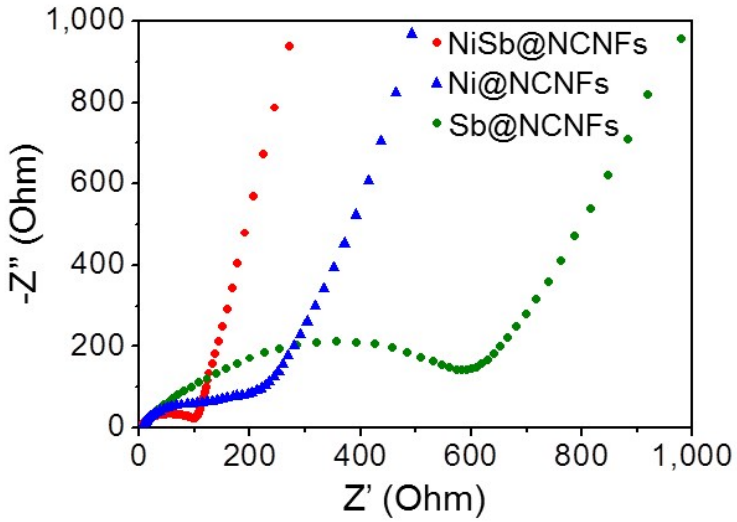

Fig. S6 Nyquist plots of NiSb@NCNFs, Ni@NCNFs and Sb@NCNFs electrodes before cycling.

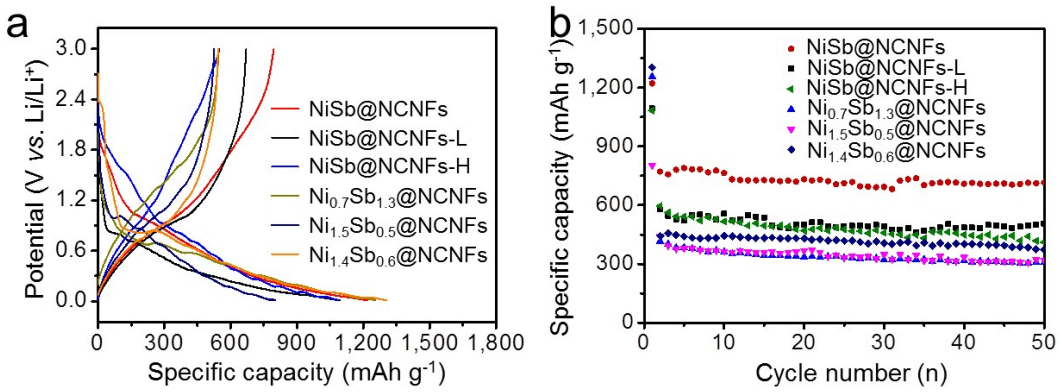

Fig. S7 (a) Discharge and charge profiles in the initial cycle and (b) Cyclic performance comparision of the NiSb@NCNFs, NiSb@NCNFs-L, NiSb@NCNFs-H, $Ni_{0.7}Sb_{1.3}$@NCNFs, $Ni_{1.5}Sb_{0.5}$@NCNFs and $Ni_{1.4}Sb_{0.6}$@NCNFs electrodes at a current density of 100 mA g^{-1}. The NiSb@NCNFs-L and NiSb@NCNFs-H electrodes were obtained by changing the weight contents of NiSb to 35.2 wt.% and 53.6 wt.%, respectively. The Ni_xSb_y@NCNFs electrodes were obtained by changing the molar ratio of Ni and Sb precursors in the PAN/DMF solution, in which the ratio of x:y were the mole ratio of Ni:Sb, while the total moles of Ni and Sb were fixed at 6.0 mmol.

Two control samples with different NiSb contents were fabricated by changing the weight contents of $SbCl_3$ and $NiCl_2{\cdot}6H_2O$ precursors in the PAN/DMF solution (while the mole ratio of Ni and Sb precursors was still 1:1), which were denoted as NiSb@NCNFs-L (low content, 35.2 wt.%) and NiSb@NCNFs-H (high content, 53.6 wt.%), respectively. The mass contents of the NiSb in the NiSb@NCNFs-L and NiSb@NCNFs-H were measured and confirmed by ICP-OES. Moreover, another three control samples of Ni_xSb_y@NCNFs electrodes were obtained by changing the molar ratio of Ni:Sb precursors to x:y instead of 1:1, while the total moles of Ni and Sb were fixed at 6.0 mmol. Fig. S7 presents the discharge/charge profiles and cyclic performance comparison of NiSb@NCNFs, NiSb@NCNFs-L, NiSb@NCNFs-H, $Ni_{0.7}Sb_{1.3}$@NCNFs, $Ni_{1.5}Sb_{0.5}$@NCNFs and $Ni_{1.4}Sb_{0.6}$@NCNFs electrodes. The

NiSb@NCNFs electrode delivered the best specific capacity and cycling performance. Usually, a lower content of active material would result in low specific capacity. However, other problems will be accompanied if the content of active material gets too high. As depicted in Fig. S8a-c, the morphology and microstructure of the NiSb@NCNFs-L electrode with relatively low content of NiSb are similar with that of NiSb@NCNFs (Fig. 1), but the lower NiSb content of NiSb@NCNFs-L resulted in a lower specific capacity than NiSb@NCNFs. On the other hand, when the Ni and Sb precursors were added too much, the morphology and microstructure of NiSb@NCNFs-H changed a lot (Fig. S8d-f). The outer surface of NiSb@NCNFs-H showed numerous cavities and the embedded NiSb particles became larger and inhomogeneous. Some of NiSb particles in NiSb@NCNFs-H were exposed to the surface, leading to the poor stability and low utilization ratio of active material. Therefore, the electrochemical performances of both NiSb@NCNFs-L and NiSb@NCNFs-H electrodes are inferior to NiSb@NCNFs (Fig. S7). The $Ni_{0.7}Sb_{1.3}$@NCNFs, $Ni_{1.5}Sb_{0.5}$@NCNFs and $Ni_{1.4}Sb_{0.6}$@NCNFs electrodes also exhibited inferior performances to NiSb@NCNFs, which should be ascribed to the incomplete dealloying-realloying processes caused by the unequal contents of Ni and Sb.

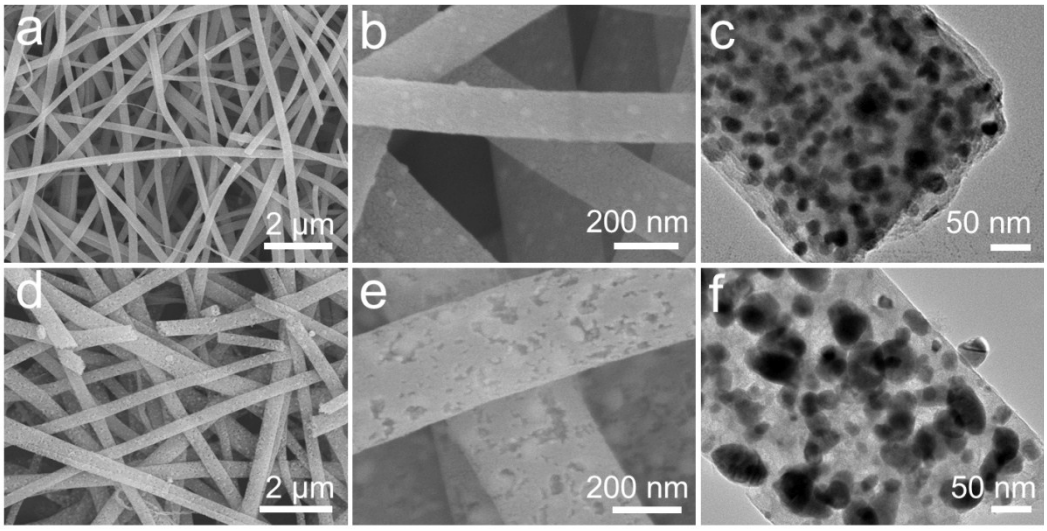

Fig. S8 (a, b) SEM and (c) TEM images of NiSb@NCNFs-L control sample. (d, e) SEM and (f) TEM images of NiSb@NCNFs-H control sample.

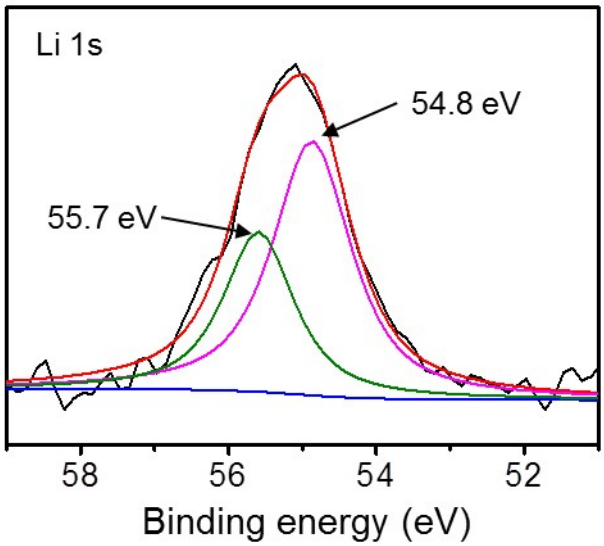

Fig. S9 High-resolution XPS spectrum at Li 1s region of NiSb@NCNFs electrode after discharge to 0.01 V.

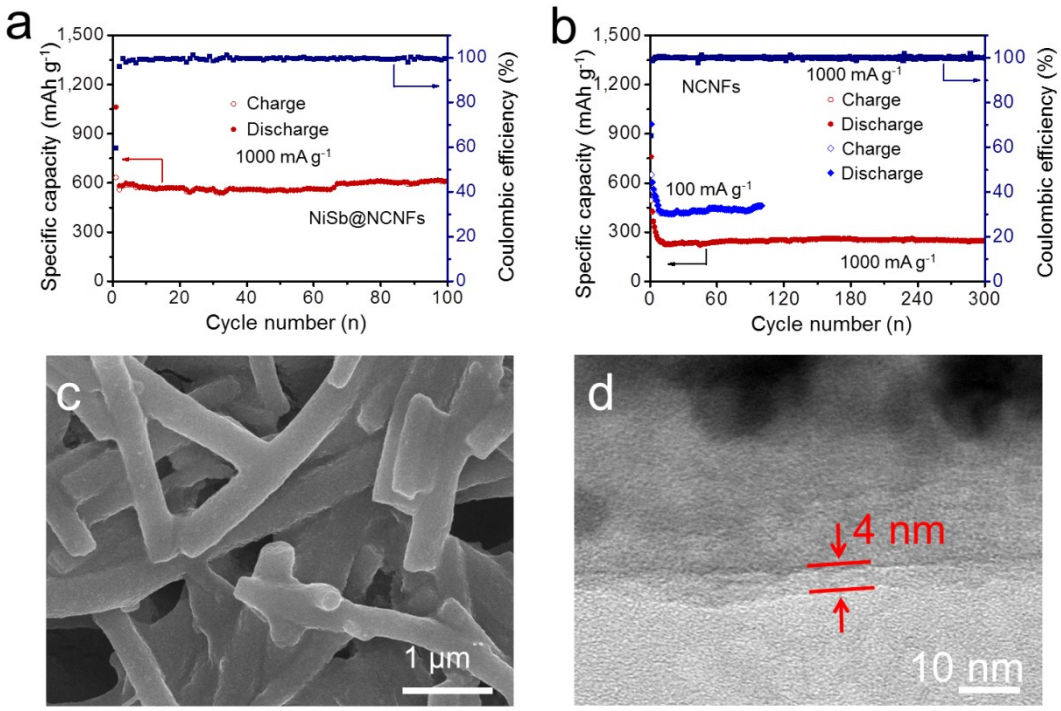

Fig. S10 (a) Cyclic performance of NiSb@NCNFs electrode at 1000 mA g^{-1}. (b) Cycle performances of pristine NCNFs control sample (without the encapsulation of NiSb nanoparticles) at 100 mA g^{-1} and 1000 mA g^{-1}. (c) SEM and (d) TEM images of NiSb@NCNFs electrode after 100 cycles at 1000 mA g^{-1}.

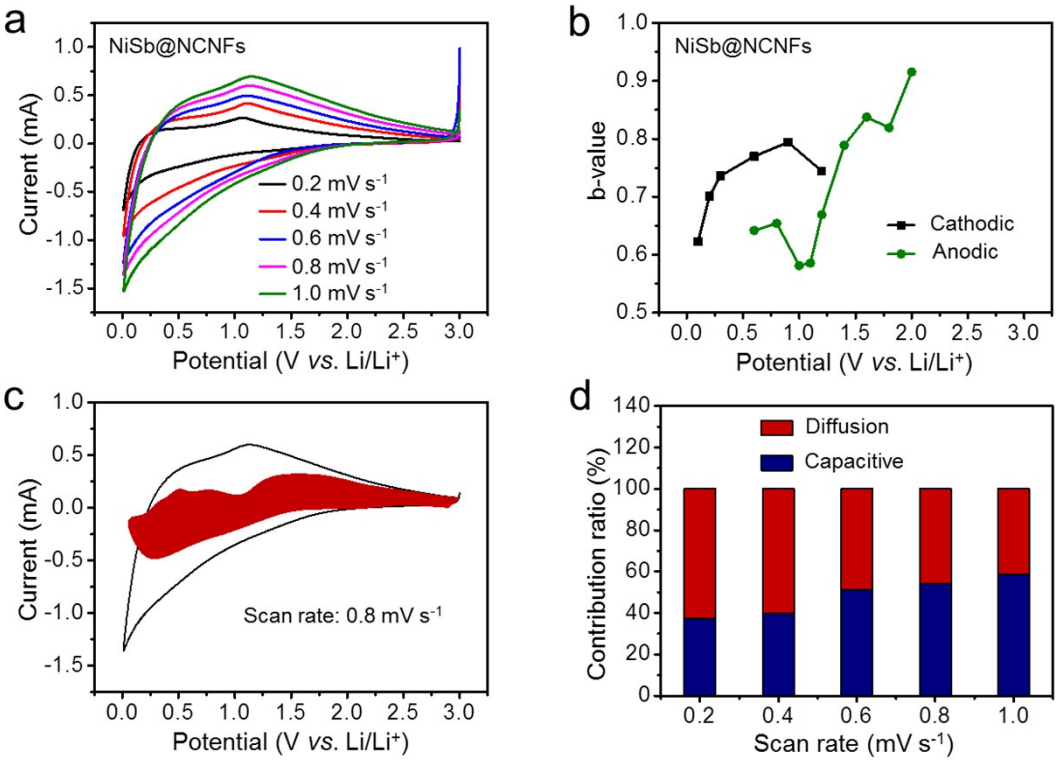

Fig. S11 (a) CV curves of NiSb@NCNFs electrode at the second discharge-charge cycle under various scan rates within 0.01–3.0 V *vs.* Li/Li^+. (b) The *b*-values of NiSb@NCNFs electrode as a function of applied potential during anodic and cathodic sweeps. (c) Contributions of diffusion and capacitive charge to the total current at the scan rate of 0.8 mV s^{-1} (the red region shows the capacitive contribution). (d) Contribution ratio of diffusion current and capacitive current at different scan rates.

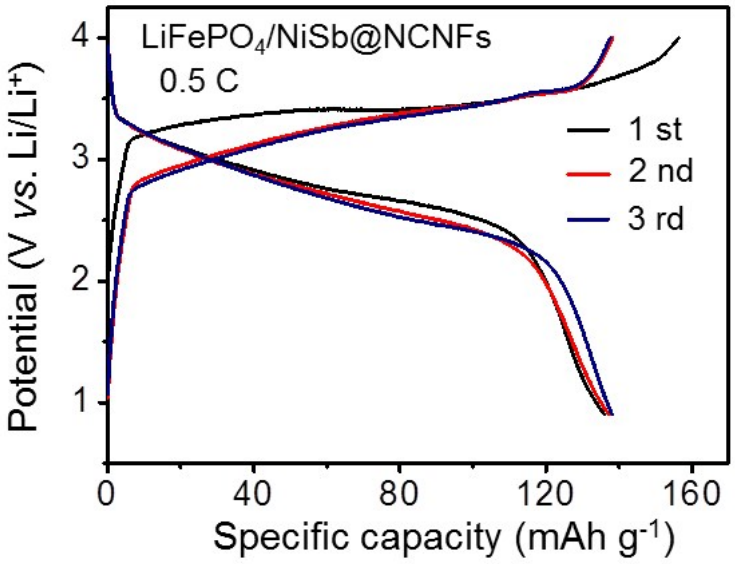

Fig. S12 Discharge-charge profiles of soft-packed full battery based on NiSb@NCNFs anode and $LiFePO_4$ cathode tested within a voltage window of 0.9–4.0 V at 0.5 C.